ACS APPLIED MATERIALS & INTERFACES

www.acsami.org

Research Article

How Hot Plasmonic Heating Can Be: Phase Transition and Melting of P25 TiO_2 from Plasmonic Heating of Au Nanoparticles

Weigang Lu,[§] Rohil Kayastha,[§] Blake Birmingham, Bernd Zechmann, and Zhenrong Zhang*

Cite This: https://doi.org/10.1021/acsami.5c03004

Read Online

ACCESS | Metrics & More | Article Recommendations | Supporting Information

ABSTRACT: Plasmonic heating has been utilized in many applications, including photocatalysis, photothermal therapy, and photocuring. However, the heat dissipation process of plasmonic nanoparticles (NPs) and the surrounding matrix is complex. How high the temperature of the matrix that surrounds the plasmonic NPs, such as the catalyst and substrate, can reach is unclear. Herein, we study the dissipation of plasmonic heat generated by resonantly excited gold (Au) NPs dispersed on a P25 TiO_2 NP porous film in air. Under resonant 532 nm continuous wave (CW) laser irradiation at the surface of Au-TiO_2, the surface evaporation and the aggregation of Au NPs were observed at moderate laser power. This process is accompanied by the phase transition of TiO_2. More importantly, the TiO_2 NP film melted, forming melt pools and a molten TiO_2 matrix. This indicates that the temperature of TiO_2 reached as high as its melting point of 1830 °C. When Au/TiO_2 was irradiated with an off-resonance laser at 638 nm, no phase transformation or melting of TiO_2 was observed. The temperature calculation showed that the heating generated by Au NPs is not localized. The collective heating from an ensemble of Au NPs in the irradiated area produced a global temperature increase that melted TiO_2. Our results suggest that the photothermal effect could be a significant mechanism in the plasmon-assisted photocatalytic reactions.

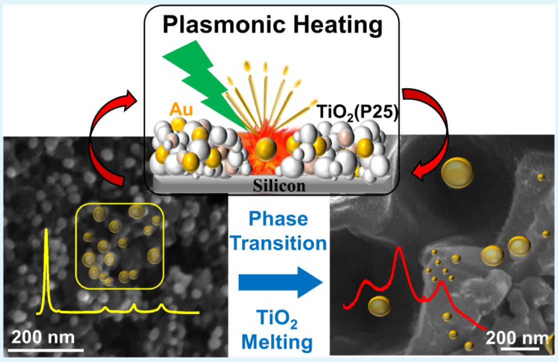

KEYWORDS: *localized surface plasmons, laser plasmonic heating, phase transition, TiO_2 melting, Au nanoparticles*

INTRODUCTION

Plasmonic heating has been utilized in various applications such as photothermal catalysis,[1,2] water evaporation,[3] photothermal therapy,[4] and epoxy photocuring.[5] Localized surface plasmon resonance (LSPR) is the phenomenon where oscillations of the conduction electrons of metallic nanoparticles (NPs) are in resonance with the oscillations of the electromagnetic field of the incident light, which significantly increases the absorption of the incoming light at the resonant frequencies.[1,6,7] The heat generated from plasmonic NPs elevates the temperature of the NPs, the surrounding media, such as air, water, and the supporting matrix, including the substrate or catalyst.[1,6,8] At the single-particle level, it has been shown that plasmonic heating can reach the melting temperature of plasmonic ZrN NPs in air.[9] Melting and surface evaporation (i.e., the ejection of tiny particles from the surface of the main particle) of Au NPs supported on a glass substrate were observed in air and in liquid.[10] The temperature increase due to plasmonic heating has been successfully simulated/estimated using the single-particle model.[9,10] However, the focus of the studies has been on plasmonic particles. The impact and mechanism of plasmonic heating on the morphology and structure of the supporting matrix/substrate have scarcely been studied, although deformation of the glass substrate has been observed. Additionally, when there is an ensemble of plasmonic particles, a discrepancy between the experimentally observed particle temperature and the temperature calculated via a single-particle model has been reported. For example, water boiling was experimentally observed when the plasmonic Au nanoparticle solution was illuminated by solar light; however, the calculated increase in temperature of the Au nanoparticle via the single-particle self-heating model was as small as 0.04 °C.[11]

The need to include collective heating for a large number of nanoparticles dispersed in a macroscopic region of material was reported back in 2006.[12] Recently, the role of collective heating in plasmonic heating has regained attention due to the difficulty in distinguishing thermal and nonthermal contributions in plasmon-driven processes.[13,14] Keblinski et al. have proposed two contributions to plasmonic heating: self-heating and collective heating.[12] Plasmonic self-heating refers to the temperature increase of a single, well-separated plasmonic NP under illumination at the plasmonic resonance. The resonance

Received: February 12, 2025
Revised: April 16, 2025
Accepted: May 6, 2025

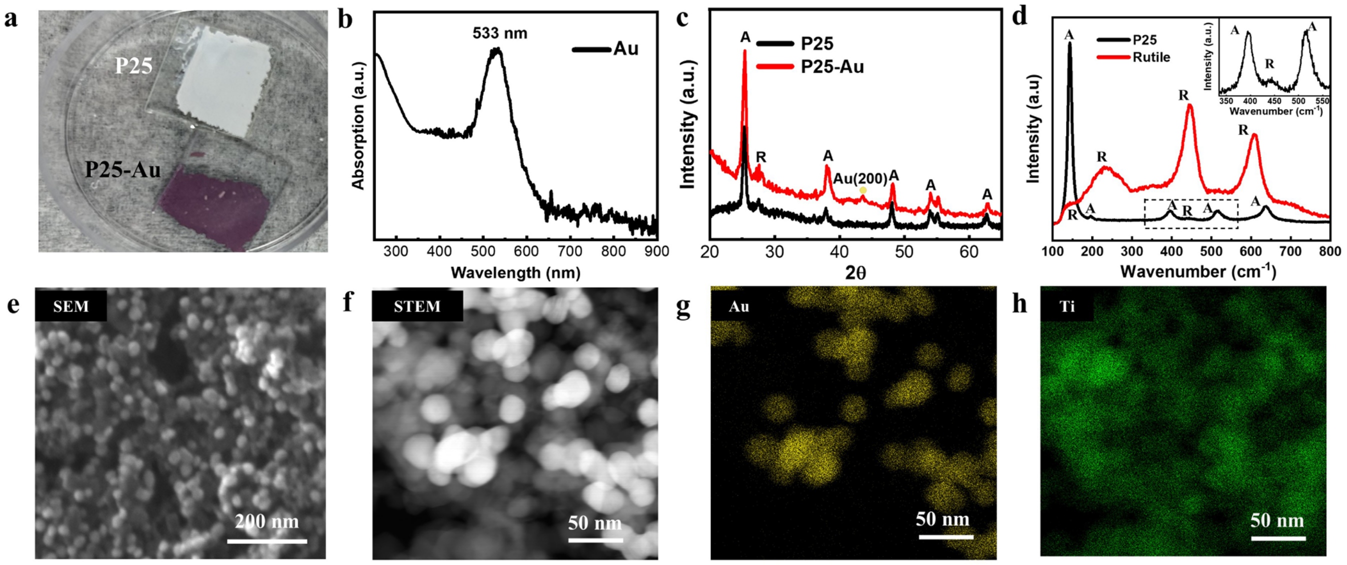

Figure 1. Characterization of the P25 TiO_2 film and the Au-decorated P25 TiO_2 film. (a) Optical image of the samples on the glass slide: P25 and P25-Au films. (b) UV–Vis of the Au NPs with a resonance at 533 nm. (c) X-ray diffraction (XRD) of the P25 and P25-Au films. (d) Raman spectra of the P25 sample and a rutile TiO_2(110) bulk crystal. The inset shows the zoomed-in spectrum of P25 in the black dashed box. (e) Scanning electron microscope (SEM) image of the P25-Au film showing a mixture of P25 (darker particles) and Au NPs (brighter particles). (f) High-angle annular dark-field scanning transmission electron microscopy (HAADF-STEM) image of the P25-Au NPs. Energy-dispersive X-ray spectroscopy (EDS) map of the image displayed in (f) showing (g) Au NPs and (h) Ti element of the P25 (TiO_2). Labels: R: Rutile, A: Anatase, and Au: Gold.

photoexcitation generates hot electron–hole pairs. The relaxation of the excited hot charge carriers via electron–electron and electro-phonon scattering increases the temperature of the plasmonic particle and the surrounding media.[1,6] Collective heating or global heating is the heating provided by all of the plasmonic particles in the irradiated region to the individual localized particles. Theoretical calculations showed that collective heating could increase the temperature by orders of magnitude higher for plasmonic nanoparticle assemblies than for single particles.[8,12,14] However, the measurement of the temperature of the NPs has been challenging.[14] Most of the temperature microscopy methods utilize optical spectroscopy, including Raman spectroscopy,[15−18] fluorescence antistokes emission of metal NPs,[19] and quadriwave shearing interferometry.[8] The validation of the temperature at the nanoscale requires comparison with simulations or cross-validation using different thermometry techniques.[20] For example, although the melting[13,14] and surface evaporation[14] of plasmonic NPs have been observed, the experimentally obtained melting and evaporation temperatures were much lower than the high temperature (thousands of Kelvin) predicted.[9,10,21]

Since 2010, plasmonic chemistry has become an attractive approach to enhance the photoreactivity of catalysts.[7,22] For example, plasmonic gold NPs supported on titanium dioxide (TiO_2) are widely reported to have better photocatalytic performance than pristine TiO_2 systems.[22,23] The primary mechanism of plasmon-assisted photoreactivity has long been connected to hot carriers. Recently, alternative mechanisms, such as photothermal effects and enhanced near-field interactions, have been proposed as significant contributors.[14,24−27] Theoretical studies suggest that the photothermal effect can explain the observed enhanced photocatalytic reactivity.[28,29] However, little experimental evidence showed the contribution of plasmonic heating due to the difficulty in measuring the temperature and separating plasmonic heating from other mechanisms.[14]

Degussa P25, composed of anatase and rutile nanocrystallites, is the gold standard for TiO_2 photocatalysts. Among the TiO_2 polymorphs, anatase is the metastable phase, whereas rutile is the stable polymorph under ambient conditions. The anatase–rutile phase transition (ART) occurs at a wide temperature range between 400 and 1200 °C.[30] Laser-induced phase transitions have been reported using femtosecond laser,[31] and nanosecond UV lasers.[32] Anatase NPs transformed into an amorphous phase[33] or rutile phase,[34] depending on the laser and the surrounding matrix. Plasmonic heating enabled the local phase transition of an amorphous TiO_2 thin film into the anatase phase, as observed on polymeric beads coated with an Au thin film under low-power CW laser irradiation.[35] Here, plasmonic heating alone did not induce a phase transition. The heat was attributed to plasmonic heating, which was enhanced by the exothermic decomposition of the polymeric beads. In general, the melting of the surrounding media with a melting point as high as ~1800 °C has not been reported from plasmonic heating by a CW laser.

In this work, we studied the impact of the plasmonic heating generated by Au NPs on the surrounding photocatalyst support, specifically the TiO_2 (Degussa P25) NP thin film. We investigated the phase transition and melting of the TiO_2 NP thin film and the surface evaporation of Au under different laser powers, both on and off the plasmonic resonance. The temperature of Au and TiO_2 NPs was compared to the calculated temperature using the established theoretical model, considering self-heating and collective heating. The temperature was also directly measured using Raman spectroscopy. The results raised questions about the high transient temperatures that Au and TiO_2 experienced during the photocatalytic reactions.

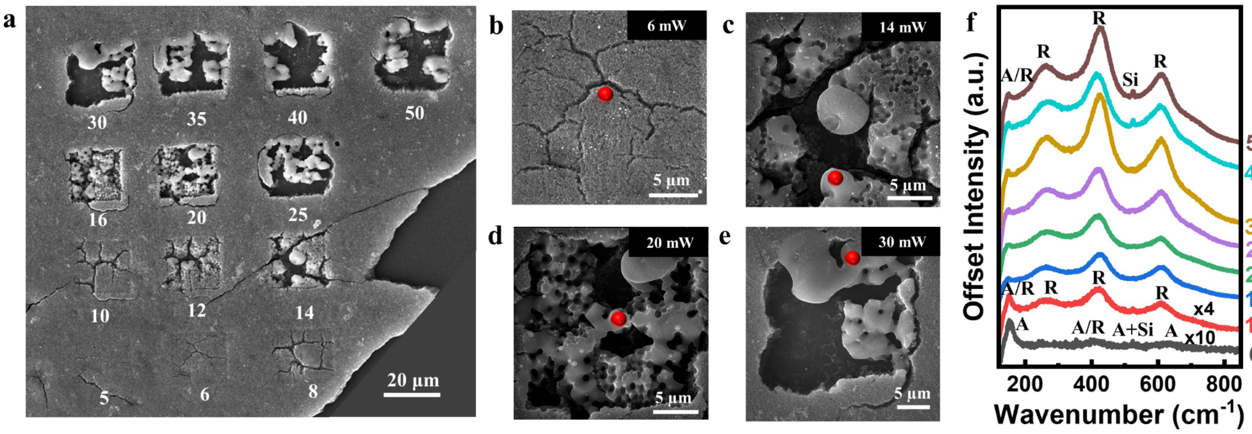

Figure 2. Characterization of the P25-Au film (600 Au NPs/μm^2) after on-resonance laser irradiation. (a) SEM image of Au-decorated P25 film after irradiation with a 532 nm CW laser at different laser powers. The white colored numbers correspond to laser power in milliwatts (mW). Zoomed-in SEM images for the areas experienced various laser powers: (b) 6 mW, (c) 14 mW, (d) 20 mW, and (e) 30 mW. Raman spectra of different spots marked as red dots in (b) to (e) are shown in (f) along with other scanned areas at various laser powers. Labels: R: Rutile, A: Anatase, and Si: Silicon. The intensities of 6 and 10 mW Raman spectra were multiplied by 10 and 4 times, respectively, to compare with the other spectra.

RESULTS AND DISCUSSION

P25 film, consisting of anatase and rutile TiO_2 NPs, was used as a support to test the effects of plasmonic heating in this study. The sample preparation and characterization are described in the Methods section. After the Au NPs decorated the P25 film, the white P25 sample turned darker red (Figure 1a). The LSPR absorption of the Au nanoparticles was at 533 nm (Figure 1b); thus, the reflection of a rich red color was observed.[36] The 532 nm wavelength laser source was chosen for maximum resonance absorption in the plasmonic heating study. The sizes of the Au NPs were around 25−30 nm (Figure S1). The average size of the P25 NPs was around 27 nm, measured from the transmission electron microscopy (TEM) images. XRD patterns (Figure 1c) of P25 and P25-Au thin films match the characteristic patterns of P25 and FCC gold NPs.[37,38] The P25 was a mixture of anatase nanocrystals (∼80%), rutile nanocrystals (15%), and a small amount of amorphous TiO_2[38]; thus, anatase and rutile peaks were observed in the XRD. The crystal structure of the TiO_2 NPs was measured by using Raman spectroscopy. The Raman spectra of the P25 and the rutile phase of TiO_2 (Figure 1d) matched the reference spectra from previous reports.[39,40] The Raman spectrum of P25 exhibits a combination of anatase and rutile peaks (Figure 1d, black curve). The peaks of the anatase vibrational spectrum can be observed at 143 cm^{-1} (E_g mode), 195 cm^{-1} (E_g mode), 396 cm^{-1} (B_{1g} mode), 517 cm^{-1} (A_{1g} mode), and 638 cm^{1} (E_g mode),[41,42] and the rutile E_g mode at 446 cm^{-1} as shown in the inset. The rutile peaks (Figure 1d, red curve) at 143, 446, and 608 cm^{-1} are assigned to the B_{1g}, E_g, and A_{1g} symmetric modes, respectively.[39,41,42] The broad peak at 239 cm^{-1} was associated with disorder-induced scattering or second-order effect in the rutile spectra.[39,42]

When the Au NPs were attached to the P25 thin film, the SEM image (Figure 1e) showed that the Au NPs were distributed uniformly but randomly on the TiO_2 porous film. Here, the Au and P25 NPs correspond to brighter and darker particles. The estimated Au nanoparticle density from SEM images was about 600/μm^2 (Figure S2). The elemental composition image of the P25-Au film was obtained using HAADF-STEM (Figure 1f), showing the composition of the P25-Au mixture. The elemental composition from the EDS map verified that the actual particles, Au (Figure 1g) and Ti (Figure 1h), from TiO_2 NPs present in the mixture match the spatial distribution of TiO_2 and Au NPs from the HAADF image.

The impact of plasmonic heating with a 532 nm laser source on the morphology and structure of the P25-Au sample is presented in Figure 2. The P25-Au film on a silicon substrate was irradiated by scanning a 20 × 20 μm^2 area with the laser beam for 500 ms exposure. The Raman map of the area was simultaneously collected during the scan. The SEM image (Figure 2a) of the P25-Au surface after laser irradiation with various increasing laser power values shows that the heat generated during the scan causes dramatic changes in the morphology of the scanned areas. At lower power (6 mW), cracks formed on the surface (Figure 2b). As the laser power increased, the size and depth of the cracks became more extensive (Figure 2a), and the formation of holes/melted pools and molten balls of TiO_2 was also observed (Figure 2c,d). The Raman spectrum (Figure 2f) at 6 mW power showed that P25 remained almost unchanged (black curve, Figure 1d). The P25 nanocrystal structure gradually transformed from mainly anatase to mainly rutile phase as more rutile peaks were observed (Figure 2f). In addition to the ART phase transition, agglomerations of melted TiO_2 were seen at higher power (>∼12 mW, Figure 2c−e). The exposed area of the Si surface also increased as the melted TiO_2 and Au NP aggregates have a higher pack density than that of the TiO_2/Au NP porous film (Figure S3). The results suggest that the melting temperature (∼1830 °C) of the TiO_2 NPs was reached due to the dissipation of plasmonic heating as the laser power increased. More details on these effects of plasmonic heating are explained in a later section. It is known that the melting temperature of NPs is much lower than the melting temperature of bulk materials. Here, the melting point of ∼1830 °C is the melting temperature of TiO_2 reagent-grade powder,[43,44] not the melting temperature of bulk TiO_2. This temperature is consistent with the calculated melting point of TiO_2 NPs with a size of 27 nm.[45] For comparison, the sintering of P25 and P25-Au films on the Si substrate was carried out separately in a muffle oven. No indication of melting was

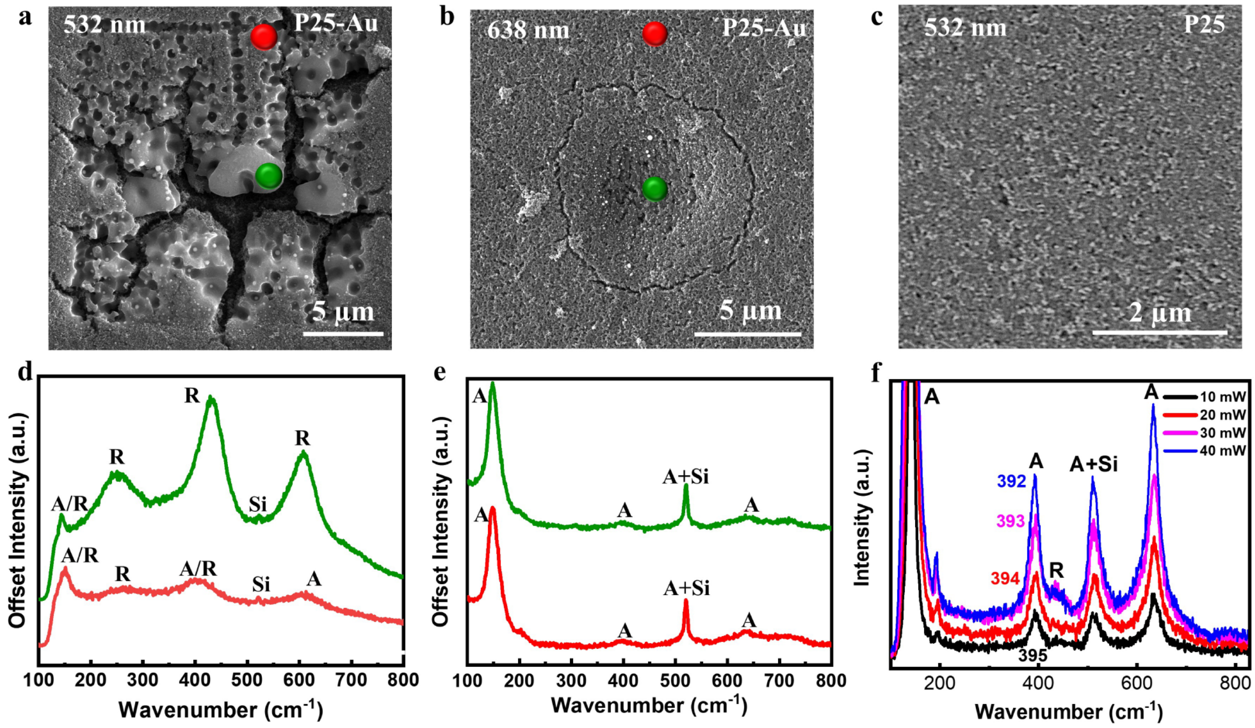

Figure 3. Characterization of P25 film and P25-Au film (600 Au NPs/μm^2) with on-resonance (532 nm) and off-resonance (638 nm) laser irradiation. SEM images of P25-Au film after laser scanning: (a) 532 nm at 12 mW and (b) 638 nm at 18 mW powers. (c) SEM image of P25 sample after scanning with 532 nm laser at 30 mW power. (d, e) Raman spectra of different spots marked as red and green dots in panels a and b, respectively. (f) Raman spectra of the P25 were taken with a 532 nm laser at various powers during scanning. The anatase peak position at 395 cm^{-1} blue-shifted as the laser power increased due to a temperature change.

observed after annealing to 1080 °C (Figure S4), which is expected from the melting temperature of TiO_2 NPs. XRD showed that anatase−rutile transition occurred in P25-Au films between 600 and 700 °C (Figure S5a), consistent with the reported P25 phase transition.[37,46−48]

In order to check whether the structural change of TiO_2 was due to the presence of LSPR, two different laser wavelengths—one on-resonance and one off-resonance with the LSPR of the Au NPs—were used to irradiate the same P25-Au sample. When an on-resonance 532 nm laser scanned the P25-Au film, the surface morphology changed, as shown above. Cracks and clumps of melted TiO_2 particles were seen in the SEM image (Figure 3a) after being irradiated at 12 mW laser power. In comparison, when an off-resonance 638 nm laser at 18 mW power (Figure 3b) was used, the surface had only small cracks in the scan area due to the laser heat. The drastic differences between the on- and off-resonance laser irradiation were also observed in an optical microscope image (Figure S6a). These effects can be more clearly understood after studying the Raman spectra, which were simultaneously obtained during the scans. At the center area (green spot) with a 532 nm scan, the cluster area had converted to a rutile phase (green curve in Figure 3d) due to intense plasmonic heat generated by the Au NPs. At the edge area (red spot), the P25 was partially converted to rutile, as both anatase/rutile phases were observed, and the rutile peak intensity was weaker compared to the center spot (red curve in Figure 3d). For the off-resonance scan, the P25 Raman spectrum (Figure 3e) showed no change. Both the center (green curve) and the edge (red curve) spectra were comparable to those of the reference P25 spectrum (black curve in Figure 1d), which was dominated by the anatase phase. Thus, confirming the critical role of LSPR resonance in the heating of the sample.

The plasmonic heating effect on the structural change of the TiO_2 film should depend on the number density of the Au NPs. Crack formation, phase transition, and melting of TiO_2 were observed when samples with a low Au particle density (∼75/μm^2) were irradiated with a 532 nm laser (Figure S7a). However, these changes occurred at powers about 10 mW higher than those required for the sample with a higher particle density (600/μm^2).

The laser itself can generate an intense amount of heat on the sample.[39,49] Here, the role and effect of laser heating alone were studied by measuring the power-dependent Raman spectra of the P25 thin film without Au NPs. No deformation or cracks were observed on the surface (Figures 3c and S6b) when a 532 nm laser at 30 mW irradiated a thin film of the P25 sample. Raman spectra (Figure 3f) obtained at different laser powers from 10 to 40 mW show that the phase of the P25 remains mainly unchanged. Only a tiny peak at 445 cm^{-1} showed the contribution of the rutile phase. The anatase B_{1g} mode position shifted from 395 cm^{-1} to 392 cm^{-1} due to a temperature increase caused by laser irradiation, which is far lower than the ART-required temperature of 600−700 °C for P25. Our results showed that plasmonic NPs, Au in this case, and an on-resonance wavelength irradiation were responsible for the observed phase transition and melting of the P25 NPs.

This section presents a detailed study of the impact of plasmonic heating on the morphological changes in TiO_2 and Au NPs on the sample with a higher Au particle density (600/μm^2), as observed from SEM, TEM, and EDS images. At 8 mW power, fractures and cracks began to form, as seen in a lower magnification SEM image (Figure 4a). At the crack's

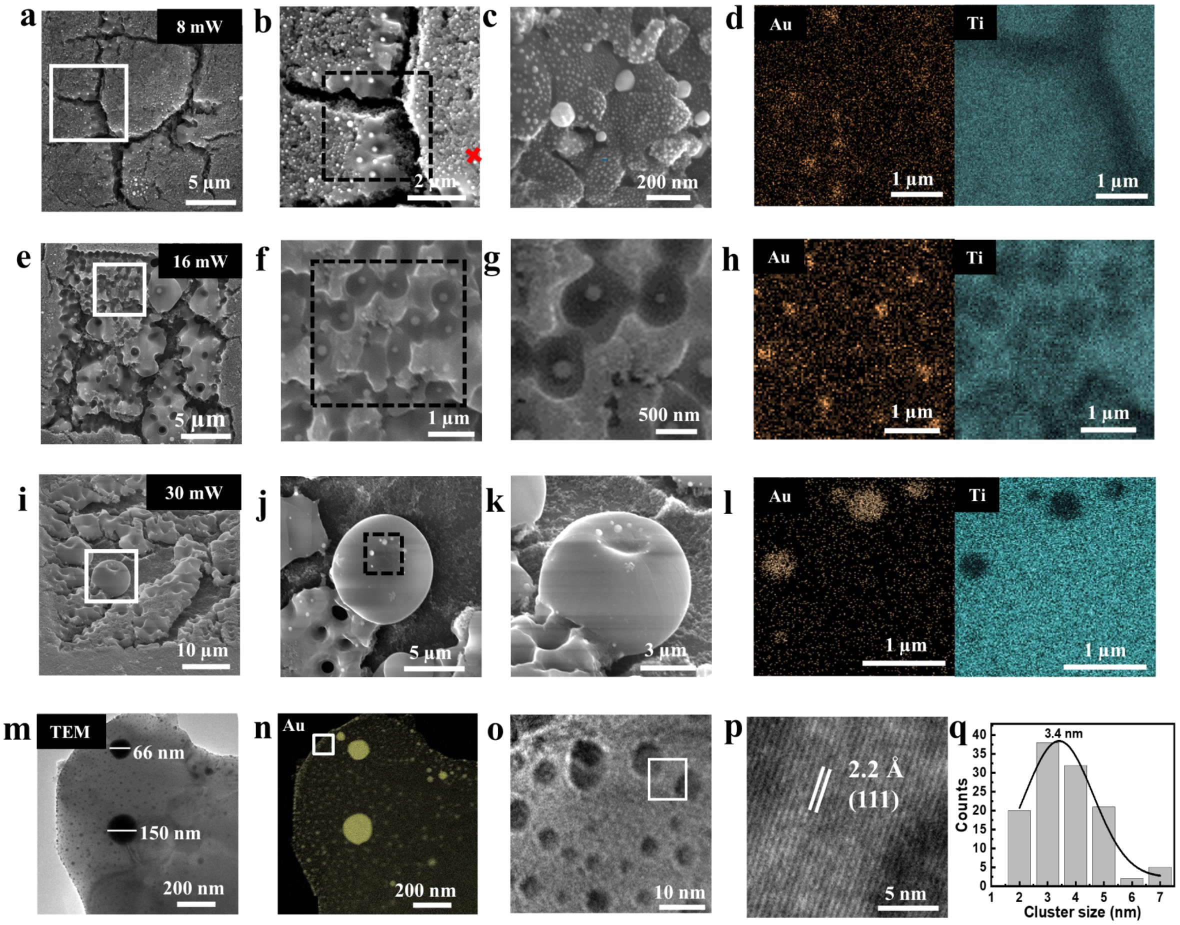

Figure 4. Detailed characterization of the P25-Au film (600 Au NPs/μm^2) after on-resonance laser scanning. SEM image of the irradiated area with 532 nm laser at powers (a) 8 mW, (e) 16 mW, and (i) 30 mW. Zoomed-in SEM image of the white square showing various effects of plasmonic heating seen at different laser powers: (b) surface cracks at 8 mW power, (f) melted pools of TiO_2 at 16 mW power, and (j) melted TiO_2 ball at 30 mW. (d, h, and l) The EDS image of Au and Ti elements from the black box square in panels (b), (f), and (j), respectively. High-magnification images showing (c) evaporated and sintered Au NPs from the red cross marked area in (b); (g) melted TiO_2 pools with an Au nanoparticle at the center of pools from panel (f); (k) side view of the melted ball-shaped TiO_2 in panel (j). (m) TEM image of the P25-Au mixture after irradiation with 16 mW laser power, where the darker spots are Au NPs. (n) Au elemental map from STEM of (a). (o) The zoomed-in area marked with the white square in panel (n) shows the size and the distribution of evaporated Au NPs. (p) The high-resolution TEM image of the white square marked area in panel (o) shows the laser-induced rutile phase. (q) Size distribution chart of evaporated Au NPs from the TEM image.

edge (Figure 4b), a smooth layer of TiO_2 can be observed along with Au particles embedded in the TiO_2 matrix. The EDS image (Figure 4d) of Au and Ti of that area verified that the NPs embedded are indeed Au particles. Those Au NPs are much larger (~100−200 nm) than the particles in the area without the crack. Further investigation into the area without cracks at higher magnification and resolution (red cross in Figure 4b) revealed two variations in the size of the Au nanoparticles, as shown in Figure 4c. The larger particles of ~50−100 nm were formed from the sintering of the Au NPs, and the smaller particles were less than 10 nm in size. The smaller particles indicate the ejection of small particles from the original Au NPs at the surface evaporation temperature or boiling point. This observation is consistent with the CW-laser-induced surface evaporation of the Au NPs in air supported on glass.[10] The estimated temperature for the surface evaporation (1200 − 2350 °C) was below the boiling temperature (~2830 °C) of bulk Au.[10]

Melting of TiO_2 NPs was observed as the laser power increased. At 16 mW power, aggregations and small pools of melted TiO_2 were seen (Figure 4e). Investigating further by examining the melt pools on the left side of the scan area (white box in Figure 4e), each melt pool contained an Au nanoparticle in the middle, with a size varying from 50 to 100 nm (Figure 4f−h). The size of the melted pools was close to the laser beam spot size (0.7 μm), indicating that the on-resonance wavelength Gaussian laser beam melted TiO_2 and formed sintered Au NPs at the center of the melted TiO_2 pools. The melt pool temperature was at least as high as the melting temperature of the TiO_2 NPs, which is known to be around 1830 °C.[43,45,50] Another phenomenon is the balling effect during laser melting. A molten ball of TiO_2 (Figure 4i-l) was observed after a 30 mW laser power irradiation. When the adhesion between TiO_2 and the silicon substrate weakens, the melted TiO_2 forms a ball instead of adhering to the surface, minimizing the surface energy. This is known as the balling effect, commonly observed in laser powder-bed fusion additive manufacturing.[51] At different laser powers, sintered Au NPs were also seen embedded in the TiO_2 matrix (Figure S8). The ball-shaped TiO_2, melted pools of TiO_2, and evaporation of Au indicate that the temperature due to plasmonic heating reached at least as high as 1830 °C.

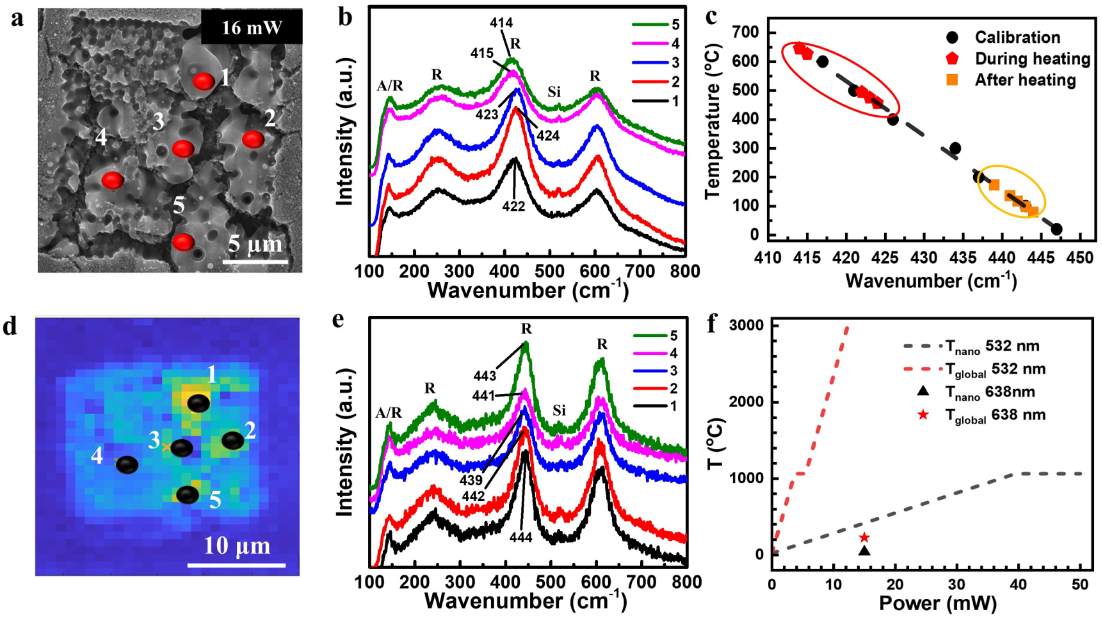

Figure 5. Investigation of temperature changes due to plasmonic heating. (a) SEM image of the plasmonically heated area with 16 mW laser irradiation. (b) Raman spectra of 5 different spots (red) highlighted in (a) during plasmonic heating. (c) A temperature of the plasmonically heated area during heating (red) and after heating (orange) obtained from a calibration curve (black) of the temperature vs wavelength shifts of rutile E_g peak. (d) Raman map of the plasmonically heated area (16 mW) and surrounding obtained with nondestructive 2 mW laser power after plasmonic heating. (e) Raman spectra from the same five spots (black in panel (d) as in panel (a) after heating. (f) The dependence of the temperature of Au nanoparticle on the power of 532 nm laser and 638 nm calculated based on isolated single particle self-heating (black, T_{nano}) and collective/global heating (red, T_{global}).

Further morphological changes in Au and P25 NPs were analyzed using scanning TEM. Another P25-Au film sample was irradiated with 16 mW laser power for TEM imaging. The Au−P25 mixture from a large scan area was separated from the silicon substrate and then transferred to a TEM grid for transmission imaging. A TEM image (Figure 4m) and the corresponding Au elemental image (Figure 4n) showed large sintered Au NPs and small evaporated Au NPs embedded in TiO_2. The sizes of the large, sintered Au particles were 150 and 66 nm, respectively (HAAD image and EDS map of Ti and O in Figure S9).

A zoomed-in high-resolution TEM image (Figure 4o) showed that the size of small Au NPs was less than 10 nm. The mean size of the smaller Au NPs obtained from four 50 × 50 nm^2 areas was about 3.4 ± 0.5 nm, as shown in the size distribution chart (Figure 4q). The evaporated Au NPs were distributed throughout the rutile TiO_2 matrix. The mean size of these smaller particles is about eight times smaller than the original nanoparticle size, confirming the evaporation of the Au. The surrounding TiO_2 matrix was transformed to a rutile phase due to plasmonic heating; a fringe spacing of 2.2 Å can be observed (Figure 4p), corresponding to the rutile (111) plane. For comparison, P25 and Au NPs in the P25-Au film annealed in an oven at 900 °C without laser exposure showed typical sintering and ART phenomena.[37,46−48] The average size of gold NPs increased to 80 nm, and TiO_2 NPs, after phase transition, increased to a few hundred nanometers through the aggregation of adjacent NPs (Figure S5b,c).

The temperature dependence of the shift of the Raman peak has been commonly used to measure temperature.[15−18] Surprisingly, the temperature measured by using Raman spectrometry during plasmonic heating is much lower than the expected temperature for the melting of the TiO_2 NPs. Here, a shift in the ∼446 cm^{-1} Raman peak was used to measure the change in temperature during and after irradiation of the P25-Au mixture. E_g mode (∼446 cm^{-1}) in the rutile phase has a significant frequency shift as the temperature changes.[16,18] The 20 × 20 μm^2 Raman map was simultaneously collected while an on-resonance 532 nm laser at 16 mW power (Figure 5a) irradiated the P25-Au sample. The laser exposure time at each pixel during the scan was 500 ms. Raman spectra (Figure 5b) from five different spots (marked in red) obtained during the scan show a variation in peak shifts of the E_g mode at 422, 424, 423, 415, and 414 cm^{-1}.

After completion of the 16 mW Raman map scan, the same scan area was rescanned (Figure 5d) with 2 mW laser power to check the E_g peak shift after heating. A 2 mW low power was chosen as no morphological changes were observed, ensuring there would be little change in the peak shift due to plasmonic heating. The Raman spectra (Figure 5e) for the same spots (marked in black in Figure 5d) show rutile E_g mode peak shifts at 444, 442, 439, 442, and 443 cm^{-1}. To correlate the E_g peak shifts to temperature changes, a temperature versus Raman shift plot (Figure 5c) was calibrated (black dot) by annealing a bulk rutile crystal in a Linkam cell (Figure S10). This calibration curve matches the calibration reported by Lan et al.[16] During plasmonic heating with a 16 mW laser (red marker), the temperature was recorded between 450 and 650 °C, whereas after it had cooled down, the temperature (orange marker) ranged from 50 to 150 °C. A mean 450 °C temperature difference is seen during and after the scan. The temperature was also calibrated using the stokes and antistokes Raman signals, as seen in Figure S11. The temperature range obtained during laser scanning is comparable to that obtained from the Raman peak shift. The measured temperature during laser scanning was lowered to 200−400 °C (Figure S7e) on the sample with low Au particle density (∼75/μm^2). However, the measured temperature is too low to account for the phase transition and melting of the TiO_2.

DISCUSSIONS

To understand the plasmonic heating mechanism and the discrepancy between the temperature obtained from Raman thermometry and the melting of TiO_2, the temperature of the Au NPs was calculated using plasmonic heating models.[8,12,14,52] It has been established that when illuminating an ensemble of plasmonic NPs, the heating was not necessarily localized around each NP. The temperature increase experienced at the center of the illuminated areas results from two contributions: self-heating and collective heating. Self-heating is due to the absorption of energy from light by a single particle, and an increase in its temperature can be calculated (eq 1). Under CW laser irradiation, the steady-state temperature increase of a single spherical nanoparticle of radius R from absorption of light depends on the nanoparticle's absorption cross-section (σ_{abs}), the light intensity (I), and the average thermal conductivity ($\overline{\kappa}$) of the air and the support matrix, according to[8,10,12,53]

$$\Delta T_{\mathrm{nano}} = \frac{\sigma_{\mathrm{abs}} I}{4\pi\overline{\kappa}R} \tag{1}$$

However, it has been pointed out that self-heating underestimates the temperature of the particle when multiple NPs are illuminated.[8,12,52,53] All of the NPs in the illuminated area are heated and collectively increase the temperature of the area and the particles. Collective heating or global heating could raise the temperature ($\Delta T_{\mathrm{global}}$) of the macroscopic region orders of magnitude higher than that due to self-heating (ΔT_{nano}) even under CW irradiation with moderate laser intensities.[8,12,52,53] Photothermal collective heating (eq 2) originated from heat diffusion or, in other words, the temperature field overlap with other NPs surrounding the NP. A nanoparticle j experiences additional heating from the neighboring nanoparticles i, heating their environment:[8,54]

$$\Delta T_{\mathrm{j}} = \frac{\sigma_{\mathrm{abs,j}} I}{4\pi\overline{\kappa}R_{\mathrm{j}}} + \sum_{i\neq j} \frac{\sigma_{\mathrm{abs,i}} I}{4\pi\overline{\kappa}|r_{\mathrm{i}} - r_{\mathrm{j}}|} \tag{2}$$

The second term, collective heating, can be dominant even for a sparse nanoparticle distribution. This is because the long-range temperature diffusion profile around a source of heat decays at $\delta T(r) \propto 1/r$, where r is the distance from the heat source.[54] Therefore, the contribution of the collective heating is determined by the number of particles and their interdistances in the illuminated area. The global temperature at the center of the laser beam can be estimated using the analytical equations of the theoretical model developed by Baffou et al.[8,12,14] The prediction of the temperature increase ($\Delta T_{\mathrm{global}}$) using this model was validated by comparison with numerically simulated temperatures and experimentally measured ΔT, using quadriwave shearing interferometry (QSI) designed to measure temperature distribution around nanometric heat sources,[8] optical hydrogen nanothermometry,[55] and XRD,[56] respectively. For example, the predicted $\Delta T_{\mathrm{global}}$ using an infinite lattice (Figure 5 of Baffou et al.)[8] was consistent with the measurements for a sample consisting of uniformly distributed lithographic Au NPs covering a whole one-inch glass substrate.

The Baffou et al. theory suggests that the ratio of contributions between self-heating and collective heating can be estimated using a dimensionless number $\zeta = \Delta T_{\mathrm{nano}}/\Delta T_{\mathrm{global}} = \frac{p^2}{3RH}$, where p is the mean first-neighbor particle distance, R is the radius of the plasmonic NP, and H is the characteristic size of the illuminated area.[4] For Gaussian illumination, H is the full width at half-maximum (FWHM) of the beam. For example, a value of $\zeta = 0.1$ under CW illumination indicates that $\Delta T_{\mathrm{global}}$ is 10 times ΔT_{nano}.

For the sample with a high Au particle density (600 NPs/μm^2), a small value (0.08) of ζ indicates that collective heating dominates. ζ is estimated with $R = 15$ nm, $p = 40$ nm, and $H = 400$ nm, where p is estimated from the Au NP density. The FWHM of the beam, H, is obtained by assuming a Gaussian beam profile and using experimental optical parameters (NA = 0.50).

Next, we estimate the temperature increases ΔT_{nano} and $\Delta T_{\mathrm{global}}$ of Au NPs supported on TiO_2. The temperature of a single Au nanoparticle can be estimated by using eq 1. The laser intensity I can be expressed as[10,21,57]

$$I = \frac{P(2.3546)^2}{2\pi H^2} \tag{3}$$

P denotes the power, and H is the FWHM of the laser beam. The σ_{abs} of a 30 nm diameter Au nanoparticle decorated on a TiO_2 powder film can be estimated using Mie theory with a refractive index (RI) of ∼2.60 and 1.0003 for TiO_2 and air, respectively.[58] The value of σ_{abs} (∼1280 nm^2) for the 532 nm laser is much higher than that (60 nm^2) for the 638 nm laser, as the resonance of the Au NPs is at 533 nm. The value of thermal conductivity ($\overline{\kappa}$) is taken as $\overline{\kappa} \approx \frac{\kappa_{\mathrm{TiO2}} + \kappa_{\mathrm{air}}}{2} = \frac{2 + 0.03}{2}\mathrm{W/mK} = 1.0\ \mathrm{W/mK}$. Here, the experimental value of $\overline{\kappa}$ of a dense polycrystalline TiO_2 nanoparticle film[59,60] is used for that of the P25 film. The temperature of a single Au particle (T_{nano}) is shown in Figure 5f. The temperature increase was 395 K for 532 nm and 19 K for 638 nm laser irradiation with 15 mW power and 0.4 μm FWHM beam size (∼5.8 × 10^5 W/cm^2 or 58 mW/μm^2 from eq 3). The temperature increase from the resonance (532 nm) irradiation is about 20 times that from the nonresonance (638 nm) irradiation. However, this rise in temperature from a single Au nanoparticle could not account for the observed Au surface evaporation and melting of the TiO_2 NPs, even under resonance irradiation. In another study using similar CW laser irradiance, Setoura et al. observed the surface evaporation of Au NPs into satellite NPs when well-dispersed (>10 μm apart) single Au NPs with a 100 nm diameter were irradiated on glass.[10] The estimated single-particle temperature is about 1 order of magnitude higher than the single-particle temperature estimated in our study. This is because the thermal conductivity of glass is much less than that of TiO_2. The effective $\overline{\kappa}$ (0.2 W/mK for the air/glass interface) is about five times smaller than that for the air/TiO_2 interface. Additionally, the larger particle (100 nm in diameter) has an order of magnitude larger cross-section than the 30 nm Au particles. The collective heating effect was not considered in Setoura et al.'s work because of the significant separation (10 μm) between the particles.

When collective heating is considered, the temperature increase ($\Delta T_{\mathrm{global}}$) at the center of the illuminated area with an ensemble of Au NPs on TiO_2 can be estimated from the second term in eq 2,[8] which sums up the contribution of all the

https://doi.org/10.1021/acsami.5c03004
ACS Appl. Mater. Interfaces XXXX, XXX, XXX−XXX

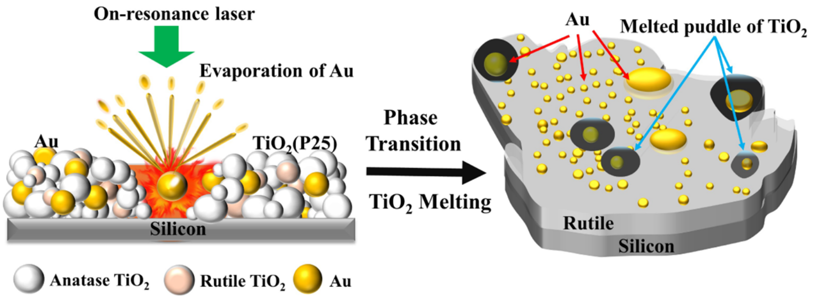

Figure 6. Mechanism of plasmonic heating induced phase transition and melting of the TiO_2 on the P25-Au film. Left: plasmonic Au NPs absorb light energy, and heat from Au NPs is dispatched to the surrounding TiO_2 medium. Melting, sintering, and vaporization of Au NPs occurred simultaneously. Right: Au clusters and Au NPs embedded in rutile phase TiO_2 after cooling.

heat generated by the NPs in the irradiation area. A Gaussian CW laser illumination of an infinite particle array yields,

$$\Delta T_{\mathrm{global}} = \frac{\sigma_{\mathrm{abs}} P}{\bar{\kappa} H A}\sqrt{\frac{\ln 2}{4\pi}}\left(1 - \frac{4\sqrt{(\ln 2)A}}{\pi H}\right) \tag{4}$$

where A is the area of the unit cell, i.e., the average area that a particle occupies, and H is the FWHM of the Gaussian beam.[8] The equation for the infinite array is chosen for our estimation because the Au NPs are dispersed over the whole TiO_2 film, which is much larger than the illumination area. Note that we use the average area of randomly dispersed particles for A.

As shown in Figure 5f, when the power is greater than 12 mW (i.e., 46 mW/μm^2), the estimated global temperature (eq 4) of the Au nanoparticle can reach the bulk boiling temperature, ~2800 °C, which is higher than that of the Au NPs. The melting enthalpy (1.22×10^9 J m^{-3}) at 1044 °C was added to the estimation. This temperature increase is an order of magnitude higher than the increase due to self-heating at the plasmonic resonance. The collective temperature increase is about 1 K per 0.002 mW/μm^2. At such a high particle temperature, it is unsurprising that we observed the formation of small (~3 nm) Au NPs, which were expected from the surface evaporation of the plasmonic Au NPs. This observation was similar to the surface evaporation of the Au NPs at the air/glass interface observed by Setoura et al.[10] Orders of magnitude higher temperatures than the estimated self-heating temperature were observed in the case of water boiling when solar light illuminated a solution of highly concentrated gold NPs.[11] Baffou et al. suggested that collective thermal effects must be considered to account for the contradiction between the experimental observation of water boiling and the small temperature increase estimated using self-heating.[14]

At low Au NP density (~75/μm^2) with 30 nm Au NPs, the estimation (Figure S7f) shows that the power required to reach the melting temperature of TiO_2 is higher than 50 mW. However, the power exhibits considerable variation depending on the particle size and particle density. The global temperature can reach the melting temperature of TiO_2 with a slightly larger average particle size (40 nm) and a slightly larger particle density (~120/μm^2) at 17 mW. This makes it reasonable to observe the melting of TiO_2 on the sample with a low Au NP density, as the particle size and the particle dispersion on the surface at a low Au NP density (Figure S7b) were not as uniform as those of the sample with a high Au NP density. The local variation in NP size and density makes it difficult to compare the estimated global temperature directly with the experimental observation.

Figure 6 shows the proposed melting process of TiO_2 due to plasmonic heating. When Au plasmonic NPs supported on a TiO_2 porous nanoparticle thin film were irradiated by a CW-laser at the plasmonic wavelength, the temperature of the Au NPs increased as a result of both localized self-heating and collective heating. When the CW laser was switched on, the time evolution of the single particle to reach the equilibrium temperature was estimated to be on the order of 0.07 ns ($\tau_{\mathrm{nano}} = {r_{\mathrm{p}}}^2/D \sim 0.07$ ns, using the thermal diffusivity of TiO_2 $D = 3 \times 10^{-6}$ m^2/s and $r_{\mathrm{p}} = 15$ nm).[10,12] The time scale for thermal fields to overlap between neighboring particles (distance between particles, d_{pp}) with a particle density of 600 particles/μm^2 can be estimated as $\tau_0 = {d_{\mathrm{pp}}}^2/D \sim 0.5$ ns, which is about seven times the time scale for a single particle to reach equilibrium temperature. The time scale for heat diffusion across the laser beam ($L = 0.7 \times 0.7$ μm^2) is $\tau_{\mathrm{global}} = L^2/D \sim 0.16$ μs. This indicates that the laser-irradiated area can reach a temperature as high as the bulk boiling point (~2800 °C) of Au at a laser power greater than 12 mW or reach the surface evaporation temperature at a lower laser power in about 0.16 μs. This time is much faster than the integration time (500 ms) used to record Raman spectra. After the temperature reached the evaporation temperature of Au, the heat dissipation and structural evolution process of the Au-TiO_2 matrix became complex. The following are the proposed mechanisms. The Au particles evaporated at the surface and splattered gold droplets with a size of ~3 nm into the surrounding area. Explosive evaporation[10] is expected at higher power (>12 mW). The heat dissipation melted the TiO_2 NPs in the laser beam, forming a liquid TiO_2 phase mixed with Au NPs. The melting of TiO_2 would cool the temperature of the mixture. The evaporation of Au reduced the particle size of individual Au particles. This changes the plasmonic resonance of Au NPs and lowers the absorption cross-section, thereby slowing down the heating rate. The Au NPs with reduced size diffused and sintered into bigger spherical Au particles (e.g., ~100 nm at 16 mW). As Au is heavier than TiO_2, large Au particles sank into the liquid pool of TiO_2. The sintering would further change the absorption cross-section for self-heating and reduce the number of particles contributing to the collective heating. Therefore, the plasmonic heating process is self-destructive once the temperature reaches the evaporation temperature of the Au NPs. The temperature estimation after evaporation (surface or explosive) requires simulations that include these complicated processes, but are beyond the scope of the current study.

The collective heating due to plasmonic absorption impacts various applications, including plasmon photochemistry, which has become a hot topic, and powder-bed additive manufacturing (AM), which has yet to be explored. The relative thermal and nonthermal contributions (e.g., hot carriers) in the plasmon-driven process have been under extensive debate regarding the application of photocatalysis.[14,24−27] The distinguishing factor requires accurately measuring the actual temperature of the plasmonic particle and the surrounding matrix (e.g., TiO_2). From shape-changing and surface evaporation, it is known that the temperature of the Au NPs and other plasmonic particles can reach their melting and boiling temperatures under moderate laser irradiance. Theoretical simulations have predicted these high temperatures.[9] However, the impact of plasmonic heating on the surrounding catalysts and the photocatalytic reaction remains unclear. Different approaches have been developed to measure the temperature accurately. Most of the developed techniques are based on optical measurements, as stated in the introduction. The time needed to take a spectrum is about 10−100 ms, which is longer than the τ_{global} (~0.2 μs) for a focused CW laser beam and the τ_{global} (~130 μs) for an unfocused CW laser beam (e.g., 20 μm diameter in air). The temperature measured from the optical spectroscopy is a time average of the temperature from rising to partially cooling down. Therefore, the temperature measured from the optical measurements does not capture the maximum temperature reached by the Au and TiO_2. Spectra were taken every 25 ms from when the laser was turned on to test this hypothesis. The E_g mode shifts (Figure S12a) from 387 cm^{-1} at 75 ms to 410 cm^{-1} at 4150 ms, representing the decay of the temperature from about 1150 to 715 °C (Figure S12b), which is too low to observe the melting of the TiO_2 NPs. Note that 25 ms is the smallest time interval for our spectrometer. A pump-and-probe experiment should be able to capture the transient temperature. Our results show that most optical methods measure the time-averaged temperature and miss the transient temperature (T_{global}) due to the collective photothermal heating, even under CW laser irradiation. Similar temperature inconsistencies have been encountered in laser-based additive manufacturing.[61] Recently, a high-speed (100 kHz) coaxial camera imaging setup has been developed to resolve the time and spatial evolution of the laser melting and melt pool cooling.[49] The time scale of the metal powder reaching the maximum temperature was about 50 μs, much less than the integration time in the Raman spectrometry.

Next, we discuss the effect of hot electron injection in the plasmonic heating of Au/TiO_2. The hot electron injection in the femtosecond laser excitation process has been shown to induce phase transitions in certain transition metal oxide semiconductors.[62−64] These semiconductors (e.g., VO_2 and perovskite manganite) belong to strongly correlated systems. Therefore, unconventional phenomena, such as nonthermal melting and semiconductor-to-metal phase transitions (SMT), can be triggered by photoexcitation without the involvement of hot carriers. Photoexcitation introduces a change in the energy distribution of excited electrons and could also coherently excite phonons needed for the phase transition via Mott and Peierls mechanisms. When plasmonic nanoparticles were added to the highly correlated systems (e.g., Au/VO_2), the injected hot electrons contributed to the phase transition of VO_2 in two mechanisms: nonthermal and thermal. Nonthermally, hot electron injection to the conduction band of the VO_2 provided an alternative mechanism, introducing a change in the electron energy distribution to trigger the SMT. Thermally, the injected hot electrons (nonthermally) to VO_2 could subsequently relax into lattice phonons via electron−phonon scattering (thermal effect), thereby increasing the temperature of the oxides. The nonthermal process dominates the phase transition of these SMT transition metal oxides due to the strong correlation of the systems.

TiO_2 is not a strongly correlated system. Therefore, we excluded the nonthermal phase transition mechanism. The hot electrons injected from Au to TiO_2 could contribute to the TiO_2 phase transition thermally. For self-heating, the heat generated via relaxation of the hot electrons was shared between the Au and TiO_2 NPs. If we assume 50% of the hot electrons generated by Au NPs were injected into TiO_2,[65] then 50% of the energy was dissipated to raise the temperature of Au NPs, and 50% of the energy was dissipated to raise the temperature of TiO_2 NPs. Therefore, the ΔT_{nano} would be less than what was estimated in Figure 5f. However, hot electron injection will not change the temperature ΔT_{global} due to the collective heating. In collective heating, an Au NP and surrounding TiO_2 NPs can be treated as one heat source, as both Au and TiO_2 NPs would contribute to the collective heat diffusion in the second term of eq 2. Therefore, the estimated temperature increase due to collective heating would be the same.

The results of this study highlight the profound effect of collective heating on the possible parameter space for CW photothermal catalysis. The temperature increase due to global heating in the catalytic reaction system (including the catalysts and molecules) can enhance the reaction rate via the thermal process in the plasmonic photocatalytic reaction. However, due to the difficulty in measuring the temperature, the thermal effect resulting from collective heating has been underestimated. In fact, Dubi et al. reported that the thermal effect could explain the reported enhanced reaction rate in plasmonic-assisted photoreactions instead of the hot-electron mechanism.[28,29] Our results show direct evidence of the difficulty of the temperature measurement, although melting of the TiO_2 was observed. The Au/TiO_2 system is a system that has been extensively studied as a plasmonic photocatalyst system.[66−68] The enhanced reaction mechanism has been widely accepted as being dominated by the plasmonic hot-carrier effect. Our work shows that plasmonic heating from CW illumination could raise the system to a higher temperature than experimentally measured, inducing phase transitions in the catalyst and enhancing reactivity thermally. The results suggest that the photothermal effect could be a significant mechanism in plasmon-assisted photocatalytic reactions.

■ CONCLUSIONS

Morphological and molecular structural effects of plasmonic heating on the Au-decorated P25 TiO_2 NP porous film have been studied. With the increase in the power of a laser whose wavelength is in resonance with the LSPR of Au NPs, the phase of P25 transformed from a mainly anatase phase to a rutile phase, accompanied by the formation of cracks and aggregates. At higher laser power, agglomerations of melted TiO_2 were observed, indicating that the matrix surrounding the Au NPs reached a temperature as high as the melting temperature of TiO_2 NPs, 1830 °C. Irradiation at the off-resonance laser wavelength did not result in a phase transition or the melting of TiO_2, which confirms the role of plasmonic heating. The calculations show that collective heating dominates the contribution to the melting of TiO_2. However, the temperature measured using Raman spectroscopy was much lower than the transient temperature that the Au and TiO_2 NPs experienced. The results suggest that optical measurements often miss the high transient temperatures that Au and TiO_2 experienced in photocatalytic reactions.

METHODS

Materials and Sample Preparation. P25 TiO_2 (purity: > 99.5%) was purchased from Sigma-Aldrich (Sigma-Aldrich, St. Louis, MO). Au NPs were synthesized using the chemical reduction of a 0.25 mM gold precursor $HAuCl_4$ by 0.25 mM trisodium citrate at 100 °C for 20 min.[69] In preparation for the P25 film, 1.5 g of P25 powder was mixed and ground well with 3 mL of ethylene glycol to form a smooth paste. This paste was then spread onto a Si or glass substrate with a blade in the space between transparent tape.[70] The thickness of the tape determined the thickness of the P25 film. The P25 films were dried overnight at 200 °C in air for 2 h and designated as-prepared P25 films. The as-prepared P25 was immersed in a gold nanoparticle aqueous solution overnight to obtain the Au-decorated P25 film, which was washed with water to remove loosely attached Au NPs and then dried overnight at 75 °C.

Characterization and Instrumentation. Laser irradiation and scanning were carried out by a lab-built confocal Raman system, which consists of a 532 nm continuous laser source with a maximum power of 55 mW and a Zaber ASR-E closed-loop microscope stage (Zaber Technologies Inc., Canada) for scanning and focusing control.[42] An Olympus (MPLFLN50X) objective lens (50×, NA = 0.50) with ~0.7 μm beam spot size was used to scan over the sample' surface, and the optical shutter of the spectrometer controlled the exposure time. Assuming a Gaussian beam profile, the calculated $1/e^2$ diameter of the focused laser beam was 0.61 μm using the optical parameters in the setup ($\lambda = 532$ nm, $M^2 = 1$, focal length of the objective = 3.6 mm, and beam diameter at the lens = 4 mm). However, experimentally, the beam profile was slightly asymmetrical, and the beam spot size of ~0.7 μm was measured from the SEM image of the individual melted TiO_2 matrix due to plasmonic heating. The FWHM of the beam was calculated to be ~0.4 μm. The movement of the stages was controlled by MATLAB codes programmed in our lab. In a typical plasmonic heating scan, the scanning area was 20 μm × 20 μm with a 40-pixel × 40-pixel resolution. The laser exposure time at each pixel was 500 ms. The laser power was adjusted with an NDC-100C-4 M filter (Thorlabs, Newton, NJ, USA). The Raman spectra were collected using a Princeton Instruments SCT-320 spectrometer with an 1800 lines/mm grating simultaneously with the laser-induced plasmonic heating. The peak of Si at 520.4 cm^{-1} was used as the calibration for all the Raman spectral analyses.

The X-ray diffraction patterns of TiO_2 and TiO_2 -Au were collected using a Siemens D5000 diffractometer (Munich, Germany) in θ–2θ mode using Cu Kα radiation ($\lambda = 1.5406$ Å) as the X-ray source (operated at 40 kV and 30 A). The scanning step size for XRD was 0.05°. Scanning electron micrographs were obtained using a Focused Ion Beam Scanning Electron Microscope (SEM; Versa 3D, Thermo Fisher, formerly FEI, Hillsboro, OR, USA) at 30 kV. Energy-dispersive X-ray spectroscopy (EDS) experiments were performed with an Octane Pro EDS detector (Ametek, Berwyn, PA, USA) to determine the elemental composition of TiO_2 patterns at 20 kV with a spot size of 7. High-resolution transmission electron micrographs of the samples were obtained using a Transmission Electron Microscope (TEM, Thermo Fisher Spectra 300C) with TEM and Scanning-TEM (STEM) imaging modes operated at 300 kV.

ASSOCIATED CONTENT

Supporting Information

The Supporting Information is available free of charge at https://pubs.acs.org/doi/10.1021/acsami.5c03004.

> Additional information in Figures S1–S6 and S8–S9 displays optical images, SEM images, TEM images, and Raman spectra; Figure S7 displays the low Au density results; Figures S10–S11 show temperature calibration results; and Figure S12 displays the time-dependent temperature shift measurements (PDF)
>
> (PDF)

AUTHOR INFORMATION

Corresponding Author

Zhenrong Zhang – *Department of Physics, Baylor University, Waco, Texas 76798, United States*; orcid.org/0000-0003-3969-2326; Email: Zhenrong_Zhang@baylor.edu

Authors

Weigang Lu – *Department of Physics, Baylor University, Waco, Texas 76798, United States*; orcid.org/0000-0002-9016-2729

Rohil Kayastha – *Department of Physics, Baylor University, Waco, Texas 76798, United States*; orcid.org/0000-0001-9316-9267

Blake Birmingham – *Department of Physics, Baylor University, Waco, Texas 76798, United States*

Bernd Zechmann – *Center for Microscopy and Imaging, Baylor University, Waco, Texas 76798, United States*

Complete contact information is available at: https://pubs.acs.org/10.1021/acsami.5c03004

Author Contributions

§W.L. and R.K. contributed equally to this paper.

Notes

The authors declare no competing financial interest.

ACKNOWLEDGMENTS

This work was supported by the National Science Foundation under Grant CHE-2247107. The authors acknowledge the support of the Center for Microscopy and Imaging at Baylor University. The authors express their gratitude to Steve Dworkin from the Department of Geosciences at Baylor University for generously granting permission to utilize the XRD equipment for this study. The authors would like to thank Lucy Lu for her contribution to image analysis.

REFERENCES

(1) Yang, B.; Li, C. Y.; Wang, Z.; Dai, Q. Thermoplasmonics in Solar Energy Conversion: Materials, Nanostructured Designs, and Applications. *Adv. Mater.* **2022**, *34* (26), 2107351.

(2) Jain, P. K. Taking the Heat Off of Plasmonic Chemistry. *J. Phys. Chem. C* **2019**, *123* (40), 24347–24351.

(3) Zhao, F.; Guo, Y. H.; Zhou, X. Y.; Shi, W.; Yu, G. H. Materials for solar-powered water evaporation. *Nat. Rev. Mater.* **2020**, *5* (5), 388−401.

(4) Xu, C.; Pu, K. Y. Second near-infrared photothermal materials for combinational nanotheranostics. *Chem. Soc. Rev.* **2021**, *50* (2), 1111−1137.

(5) Roberts, A. T.; Yang, J.; Reish, M. E.; Alabastri, A.; Halas, N. J.; Nordlander, P.; Everitt, H. O. Plasmonic nanoparticle-based epoxy photocuring: A deeper look. *Materials Today.* **2019**, *27*, 14−20.

(6) Jauffred, L.; Samadi, A.; Klingberg, H.; Bendix, P. M.; Oddershede, L. B. Plasmonic Heating of Nanostructures. *Chem. Rev.* **2019**, *119* (13), 8087−8130.

(7) Brongersma, M. L.; Halas, N. J.; Nordlander, P. Plasmon-induced hot carrier science and technology. *Nat. Nanotechnol.* **2015**, *10* (1), 25−34.

(8) Baffou, G.; Berto, P.; Ureña, E. B.; Quidant, R.; Monneret, S.; Polleux, J.; Rigneault, H. Photoinduced Heating of Nanoparticle Arrays. *ACS Nano* **2013**, *7* (8), 6478−6488.

(9) Setoura, K.; Ito, S. Quantifying the durability of transition metal nitrides in thermoplasmonics at the single-nanoparticle level. *AIP Adv.* **2021**, *11* (11), 115027.

(10) Setoura, K.; Okada, Y.; Hashimoto, S. CW-laser-induced morphological changes of a single gold nanoparticle on glass: observation of surface evaporation. *Phys. Chem. Chem. Phys.* **2014**, *16* (48), 26938−26945.

(11) Neumann, O.; Urban, A. S.; Day, J.; Lal, S.; Nordlander, P.; Halas, N. J. Solar Vapor Generation Enabled by Nanoparticles. *ACS Nano* **2013**, *7* (1), 42−49.

(12) Keblinski, P.; Cahill, D. G.; Bodapati, A.; Sullivan, C. R.; Taton, T. A. Limits of localized heating by electromagnetically excited nanoparticles. *J. Appl. Phys.* **2006**, *100* (5), 054305.

(13) Mascaretti, L.; Naldoni, A. Hot electron and thermal effects in plasmonic photocatalysis. *J. Appl. Phys.* **2020**, *128* (4), 041101.

(14) Baffou, G.; Bordacchini, I.; Baldi, A.; Quidant, R. Simple experimental procedures to distinguish photothermal from hot-carrier processes in plasmonics. *Light: Sci. Appl.* **2020**, *9* (1), 108.

(15) Huang, X.; Gao, Y.; Yang, T.; Ren, W.; Cheng, H.-M.; Lai, T. Quantitative Analysis of Temperature Dependence of Raman shift of monolayer WS_2. *Sci. Rep.* **2016**, *6* (1), 32236.

(16) Lan, T.; Tang, X.; Fultz, B. Phonon anharmonicity of rutile TiO_2 studied by Raman spectrometry and molecular dynamics simulations. *Phys. Rev. B* **2012**, *85* (9), 094305.

(17) Szymczak, M.; Piotrowski, W. M.; Woźny, P.; Runowski, M.; Marciniak, L. A highly sensitive lifetime-based luminescent manometer and bi-functional pressure−temperature sensor based on a spectral shift of the R-line of Mn^{4+} in $K_2Ge_4O_9$. *J. Mater. Chem. C* **2024**, *12* (19), 6793.

(18) Rani, C.; Pathak, D. K.; Tanwar, M.; Kandpal, S.; Ghosh, T.; Maximov, M. Y.; Kumar, R. Anharmonicity induced faster decay of hot phonons in rutile TiO_2 nanorods: a Raman spectromicroscopy study. *Mater. Adv.* **2022**, *3* (3), 1602.

(19) Carattino, A.; Caldarola, M.; Orrit, M. Gold Nanoparticles as Absolute Nanothermometers. *Nano Lett.* **2018**, *18* (2), 874.

(20) Martinez, L. P.; Mina Villarreal, M. C.; Zaza, C.; Barella, M.; Acuna, G. P.; Stefani, F. D.; Violi, I. L.; Gargiulo, J. Thermometries for Single Nanoparticles Heated with Light. *ACS Sens.* **2024**, *9* (3), 1049−1064.

(21) Setoura, K.; Werner, D.; Hashimoto, S. Optical Scattering Spectral Thermometry and Refractometry of a Single Gold Nanoparticle under CW Laser Excitation. *J. Phys. Chem. C* **2012**, *116* (29), 15458.

(22) Boerigter, C.; Campana, R.; Morabito, M.; Linic, S. Evidence and implications of direct charge excitation as the dominant mechanism in plasmon-mediated photocatalysis. *Nat. Commun.* **2016**, *7* (1), 10545.

(23) Yergaliyeva, S.; Nemkayeva, R.; Guseinov, N.; Prikhodko, O.; Arbuz, A.; Orynbay, B.; Sagidolda, Y.; Aitzhanov, M.; Ismailova, G.; Mukhametkarimov, Y. Synthesis and optical properties of Ag/Au-TiO_2 plasmonic composite thin films. *Opt. Mater. Express.* **2023**, *13* (10), 2726−2736.

(24) Hamans, R. F.; Parente, M.; Baldi, A. Super-Resolution Mapping of a Chemical Reaction Driven by Plasmonic Near-Fields. *Nano Lett.* **2021**, *21* (5), 2149.

(25) Ou, W.; Zhou, B.; Shen, J.; Lo, T. W.; Lei, D.; Li, S.; Zhong, J.; Li, Y. Y.; Lu, J. Thermal and Nonthermal Effects in Plasmon-Mediated Electrochemistry at Nanostructured Ag Electrodes. *Angew. Chem., Int. Ed.* **2020**, *132* (17), 6856−6859.

(26) Zhang, Q.; Zhou, Y.; Fu, X.; Villarreal, E.; Sun, L.; Zou, S.; Wang, H. Photothermal Effect, Local Field Dependence, and Charge Carrier Relaying Species in Plasmon-Driven Photocatalysis: A Case Study of Aerobic Nitrothiophenol Coupling Reaction. *J. Phys. Chem. C* **2019**, *123* (43), 26695.

(27) Rodio, M.; Graf, M.; Schulz, F.; Mueller, N. S.; Eich, M.; Lange, H. Experimental Evidence for Nonthermal Contributions to Plasmon-Enhanced Electrochemical Oxidation Reactions. *ACS Catal.* **2020**, *10* (3), 2345.

(28) Sivan, Y.; Un, L. W.; Dubi, Y. Assistance of metal nanoparticles in photocatalysis − nothing more than a classical heat source. *Faraday Discuss.* **2019**, *214*, 215−233.

(29) Dubi, Y.; Un, I. W.; Sivan, Y. Thermal effects − an alternative mechanism for plasmon-assisted photocatalysis. *Chem. Sci.* **2020**, *11* (19), 5017.

(30) Hanaor, D. A. H.; Sorrell, C. C. Review of the anatase to rutile phase transformation. *J. Mater. Sci.* **2011**, *46* (4), 855−874.

(31) Ma, H. L.; Yang, J. Y.; Dai, Y.; Zhang, Y. B.; Lu, B.; Ma, G. H. Raman study of phase transformation of TiO_2 rutile single crystal irradiated by infrared femtosecond laser. *Appl. Surf. Sci.* **2007**, *253* (18), 7497−7500.

(32) Dauksta, E.; Medvids, A.; Onufrijevs, P.; Shimomura, M.; Fukuda, Y.; Murakami, K. Laser-induced crystalline phase transition from rutile to anatase of niobium doped TiO_2. *Curr. Appl. Phys.* **2019**, *19* (3), 351−355.

(33) Ricci, P. C.; Casu, A.; Salis, M.; Corpino, R.; Anedda, A. Optically Controlled Phase Variation of TiO_2 Nanoparticles. *J. Phys. Chem. C* **2010**, *114* (34), 14441−14445.

(34) Ricci, P. C.; Carbonaro, C. M.; Stagi, L.; Salis, M.; Casu, A.; Enzo, S.; Delogu, F. Anatase-to-Rutile Phase Transition in TiO_2 Nanoparticles Irradiated by Visible Light. *J. Phys. Chem. C* **2013**, *117* (15), 7850−7857.

(35) Alessandri, I.; Ferroni, M.; Depero, L. E. In Situ Plasmon-Heating-induced Generation of Au/TiO_2 "Hot Spots" on Colloidal Crystals. *ChemPhyschem* **2009**, *10* (7), 1017−1022.

(36) Sapsford, K. E.; Algar, W. R.; Berti, L.; Gemmill, K. B.; Casey, B. J.; Oh, E.; Stewart, M. H.; Medintz, I. L. Functionalizing Nanoparticles with Biological Molecules: Developing Chemistries that Facilitate Nanotechnology. *Chem. Rev.* **2013**, *113* (3), 1904−2074.

(37) Wang, G.; Xu, L.; Zhang, J.; Yin, T.; Han, D. Enhanced Photocatalytic Activity of TiO_2 Powders (P25) via Calcination Treatment. *Int. J. Photoenergy* **2012**, *2012*, 265760.

(38) Jiang, X.; Manawan, M.; Feng, T.; Qian, R.; Zhao, T.; Zhou, G.; Kong, F.; Wang, Q.; Dai, S.; Pan, J. H. Anatase and rutile in evonik aeroxide P25: Heterojunctioned or individual nanoparticles? *Catal. Today.* **2018**, *300*, 12−17.

(39) Ming, L.; Yang, H.; Zhang, W.; Zeng, X.; Xiong, D.; Xu, Z.; Wang, H.; Chen, W.; Xu, X.; Wang, M.; et al. Selective laser sintering of TiO_2 nanoparticle film on plastic conductive substrate for highly efficient flexible dye-sensitized solar cell application. *J. Mater. Chem. A* **2014**, *2* (13), 4566.

(40) Machín, A.; Soto-Vázquez, L.; Colón-Cruz, C.; Valentín-Cruz, C. A.; Claudio-Serrano, G. J.; Fontánez, K.; Resto, E.; Petrescu, F. I.; Morant, C.; Márquez, F. Photocatalytic Activity of Silver-Based Biomimetics Composites. *Biomimetics* **2021**, *6* (1), 4.

(41) Fateley, W. G.; Dollish, F. R.; McDevitt, N. T.; Bentley, F. F. *Infrared and Raman Selection Rules for Molecular and Lattice Vibrations: the Correlation Method*; Wiley-Interscience: New York, N.Y., 1972.

(42) Lu, W.; Zhu, H.; Birmingham, B.; Craft, N.; Hu, J.; Park, K.; Zhang, Z. Phase transition of individual anatase TiO_2 microcrystals with large percentage of (001) facets: a Raman mapping and SEM study. *Phys. Chem. Chem. Phys.* **2023**, *25* (4), 3199.

(43) Brauer, G.; Littke, W. Melting Point and Thermal Dissociation of Titanium Dioxide. *J. Inorg. Nucl. Chem.* **1960**, *16*, 67−76.

(44) Pierre, P. D. S. S. A Note on the Melting Point of Titanium Dioxide. *J. Am. Ceram. Soc.* **1952**, *35* (7), 188−188.

(45) Guisbiers, G.; Van Overschelde, O.; Wautelet, M. Theoretical investigation of size and shape effects on the melting temperature and energy bandgap of TiO_2 nanostructures. *Appl. Phys. Lett.* **2008**, *92* (10), 103121.

(46) Boytsova, O.; Zhukova, I.; Tatarenko, A.; Shatalova, T.; Beiltiukov, A.; Eliseev, A.; Sadovnikov, A. The Anatase-to-Rutile Phase Transition in Highly Oriented Nanoparticles Array of Titania with Photocatalytic Response Changes. *Nanomaterials* **2022**, *12* (24), 4418.

(47) Byrne, C.; Fagan, R.; Hinder, S.; McCormack, D. E.; Pillai, S. C. New approach of modifying the anatase to rutile transition temperature in TiO_2 photocatalysts. *RSC Adv.* **2016**, *6* (97), 95232.

(48) Hiremath, V.; Heo, J.; Park, H.-H.; Seo, J. G. Crystallinity swayed phase transformation and oxygen vacancy formation in TiO_2 aerogel photocatalysts. *Environ. Res.* **2023**, *239*, 117409.

(49) Hooper, P. A. Melt pool temperature and cooling rates in laser powder bed fusion. *Addit. Manuf.* **2018**, *22*, 548−559.

(50) Le Ba, T.; Várady, Z. I.; Lukács, I. E.; Molnár, J.; Balczár, I. A.; Wongwises, S.; Szilágyi, I. M. Experimental investigation of rheological properties and thermal conductivity of SiO_2−P25 TiO_2 hybrid nanofluids. *J. Therm. Anal. Calorim.* **2021**, *146* (1), 493.

(51) Khairallah, S. A.; Anderson, A. T.; Rubenchik, A.; King, W. E. Laser powder-bed fusion additive manufacturing: Physics of complex melt flow and formation mechanisms of pores, spatter, and denudation zones. *Acta Mater.* **2016**, *108*, 36−45.

(52) Baldi, A.; Askes, S. H. C. Pulsed Photothermal Heterogeneous Catalysis. *ACS Catal.* **2023**, *13* (5), 3419.

(53) Baffou, G.; Quidant, R.; García de Abajo, F. J. Nanoscale Control of Optical Heating in Complex Plasmonic Systems. *ACS Nano* **2010**, *4* (2), 709−716.

(54) Baffou, G.; Cichos, F.; Quidant, R. Applications and challenges of thermoplasmonics. *Nat. Mater.* **2020**, *19* (9), 946−958.

(55) Tiburski, C.; Nugroho, F. A. A.; Langhammer, C. Optical Hydrogen Nanothermometry of Plasmonic Nanoparticles under Illumination. *ACS Nano* **2022**, *16* (4), 6233−6243.

(56) Uusitalo, M.; Strach, M.; Eriksson, G.; Dmytrenko, T.; Andersson, J.; Dahlin, A.; Hulander, M.; Andersson, M. Photothermal Properties of Solid-Supported Gold Nanorods. *Nano Lett.* **2024**, *24* (40), 12529−12535.

(57) Carlson, M. T.; Khan, A.; Richardson, H. H. Local Temperature Determination of Optically Excited Nanoparticles and Nanodots. *Nano Lett.* **2011**, *11* (3), 1061−1069.

(58) Oldenburg, S. J. *Light scattering from gold nanoshells*; Ph.D., Rice University: United States- Texas, 2000.

(59) Fang, J.; Reitz, C.; Brezesinski, T.; Nemanick, E. J.; Kang, C. B.; Tolbert, S. H.; Pilon, L. Thermal Conductivity of Highly-Ordered Mesoporous Titania Thin Films from 30 to 320 K. *J. Phys. Chem. C* **2011**, *115* (30), 14606−14614.

(60) Hopkins, P. E.; Mittal, M.; Phinney, L. M.; Grillet, A. M.; Furst, E. M. Ultra-low thermal conductivity of ellipsoidal TiO_2 nanoparticle films. *Appl. Phys. Lett.* **2011**, *99* (13), 133106.

(61) Höfflin, D.; Sauer, C.; Schiffler, A.; Manara, J.; Hartmann, J. Pixelwise high-temperature calibration for in-situ temperature measuring in powder bed fusion of metal with laser beam. *Heliyon* **2024**, *10* (7), No. e28989−e28989.

(62) Hada, M.; Zhang, D.; Casandruc, A.; Miller, R. J. D.; Hontani, Y.; Matsuo, J.; Marvel, R. E.; Haglund, R. F. Hot electron injection driven phase transitions. *Phys. Rev. B* **2012**, *86* (13), 134101.

(63) Polli, D.; Rini, M.; Wall, S.; Schoenlein, R. W.; Tomioka, Y.; Tokura, Y.; Cerullo, G.; Cavalleri, A. Coherent orbital waves in the photo-induced insulator−metal dynamics of a magnetoresistive Manganite. *Nat. Mater.* **2007**, *6* (9), 643−647.

(64) Cocker, T. L.; Titova, L. V.; Fourmaux, S.; Holloway, G.; Bandulet, H. C.; Brassard, D.; Kieffer, J. C.; El Khakani, M. A.; Hegmann, F. A. Phase diagram of the ultrafast photoinduced insulator-metal transition in vanadium dioxide. *Phys. Rev. B* **2012**, *85* (15), 155120.

(65) Furube, A.; Du, L.; Hara, K.; Katoh, R.; Tachiya, M. Ultrafast Plasmon-Induced Electron Transfer from Gold Nanodots into TiO2 Nanoparticles. *J. Am. Chem. Soc.* **2007**, *129* (48), 14852−14853.

(66) DuChene, J. S.; Tagliabue, G.; Welch, A. J.; Cheng, W.-H.; Atwater, H. A. Hot Hole Collection and Photoelectrochemical CO2 Reduction with Plasmonic Au/p-GaN Photocathodes. *Nano Lett.* **2018**, *18* (4), 2545−2550.

(67) Ho, K. H. W.; Shang, A.; Shi, F.; Lo, T. W.; Yeung, P. H.; Yu, Y. S.; Zhang, X.; Wong, K.-Y.; Lei, D. Y. Plasmonic Au/TiO2-Dumbbell-On-Film Nanocavities for High-Efficiency Hot-Carrier Generation and Extraction. *Adv. Funct. Mater.* **2018**, *28* (34), 1800383.

(68) Yu, Y.; Wijesekara, K. D.; Xi, X.; Willets, K. A. Quantifying Wavelength-Dependent Plasmonic Hot Carrier Energy Distributions at Metal/Semiconductor Interfaces. *ACS Nano* **2019**, *13* (3), 3629−3637.

(69) Turkevich, J.; Stevenson, P. C.; Hillier, J. A study of the nucleation and growth processes in the synthesis of colloidal gold. *Discuss. Faraday Soc.* **1951**, *11*, 55−75.

(70) Fitra, M.; Daut, I.; Irwanto, M.; Gomesh, N.; Irwan, Y. M. Effect of TiO_2 Thickness Dye Solar Cell on Charge Generation. *Energy Proc.* **2013**, *36*, 278−286.